TABLE OF CONTENTS (TOC)

High-performance triboelectric nanogenerator based on theoretical analysis and ferroelectric nanocomposites and its high-voltage applications
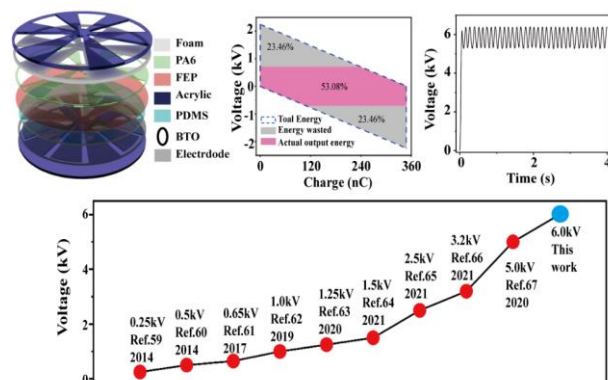
Xuhua Guo[1,3] ‡, Jianwei He[1] ‡, Yang Zheng[1], Junpeng Wu[1], Caofeng Pan[3] *, Yunlong Zi[4] *, Hongzhi Cui[1] *, Xiaoyi Li[1,2] *.

[1] Ocean University of China, China
[2] Henan University, China
[3] Beijing Institute of Nanoenergy and Nanosystems, China
[4] Hong Kong University of Science and Technology, China

A high-performance rotary triboelectric nanogenerator was fabricated using a customized air-breakdown theoretical model and a ferroelectric nanocomposite interlayer to reduce energy waste caused by air breakdown. And with the help of management circuits, the output voltage can reach 6 kV, among the best-performing triboelectric generators.

High-performance triboelectric nanogenerator based on theoretical analysis and ferroelectric nanocomposites and its high-voltage applications

Xuhua Guo[1,3,§], Jianwei He[1,§], Yang Zheng[1], Junpeng Wu[1], Caofeng Pan[3] (✉), Yunlong Zi[4] (✉),

Hongzhi Cui[1] (✉), and Xiaoyi Li[1,2] (✉)

[1] College of Materials Science and Engineering, Ocean University of China, Qingdao 266100, China
[2] Key Lab for Special Functional Materials of Ministry of Education, School of Materials Science and Engineering, Henan University, Kaifeng, 475004, China
[3] Beijing Institute of Nanoenergy and Nanosystems, Chinese Academy of Sciences, Beijing 101400, China
[4] Sustainable Energy and Environment Thrust, Hong Kong University of Science and Technology, Guangzhou, 510000, China
[§] Xuhua Guo and Jianwei He contributed equally to this work.

ABSTRACT

With the growing economy and technology, disease prevention and individual health are becoming more and more important. It is highly urgent to develop a non-toxic, self-powered, and safe high-voltage power source to prevent diseases spread by mosquitoes, especially in isolated or remote areas. Herein, we reported a high-performance rotary triboelectric nanogenerator (R-TENG) based on customized theoretical simulations and a ferroelectric nanocomposite intermediate layer. The customized theoretical simulations based on gradient electrode gaps were established to optimize gap angles and segment numbers of the electrodes, which could prevent air breakdown and enhance the R-TENG output energy by at least 1.5 times. Meanwhile, the electrical output performance of the TENG was further enhanced with a highly oriented $BaTiO_3$ (BTO) nanoparticles intermediate layer by about 2.5 times. The open-circuit voltage of R-TENG reached more than 6 kV and could continuously light 3420 LEDs or 4 serially connected 36 W household fluorescent lamps. Therefore, a self-powered high-voltage disease prevention system is developed based on the high-performance R-TENG to reduce the risk of disease transmission. This work provides a prospective strategy for the further development of TENGs and expands practical applications of self-powered and high-voltage systems.

KEYWORDS

triboelectric nanogenerator, air-breakdown, theoretical analysis, ferroelectric nanocomposite, high-voltage applications

1 Introduction

As the economy and technology develop rapidly, disease prevention and public or individual health are becoming more and more important. Numerous diseases are closely associated with mosquitoes, including malaria [1], yellow fever [2], Zika virus [3], and so on. Achieving high-efficiency mosquito-controlling systems will greatly decrease the transmission of these diseases and guarantee public or individual health. Chemical and physical methods have been two major approaches to killing mosquitoes. However, chemical methods involve toxic chemicals, which will inevitably cause serious harm to our health and environment [4, 5]. Several physical methods of mosquito-killing methods are based on high voltage. Thus, they indispensably require an external power source, which increases the system complexity, cost, and safety problems, especially in isolated islands or remote/poor areas. Therefore, it is extremely urgent to develop a self-powered system and a safe power source.

Triboelectric nanogenerators (TENGs) are one of the most promising technologies, which can convert low-frequency mechanical energy in the environment into electric power

based on Maxwell's displacement current [6–8] and TENGs have already been used for self-powered sensors/systems [9–11], environmental protection [12–14], blue energy harvesting [15–18], and so on. Due to their special characteristics of high voltage and low current, TENGs have significant advantages. Firstly, the high-voltage device based on TENG is safe. The current of TENGs is in the order of µA, which is lower than the safe current (~ mA). Then, TENGs are manufactured with existing industrial manufacturing processes, which makes TENGs enable to be integrated with other smart systems easily. Finally, TENGs are self-powered devices. They can be applied in isolated islands or remote/poor areas where it is difficult to ensure electricity supplies. Various strategies have been adopted to enhance the charge density and improve the output performance of TENGs to broaden TENG's applications, including ion implantation [19–21], triboelectric material modification [22–24], structural design [25–27], and charge chump [28, 29]. Jiang et al. increased the charge density of TENG to 50 $\mu C \cdot m^{-2}$ by introducing an intermediate layer composed of reduced graphene oxide and silver nanoparticles, which is 5 times higher than that of traditional TENG [30]. Feng et al. increased the maximum charge density of TENG to 105 $\mu C \cdot m^{-2}$ by introducing a polyimide charge storage layer between the electrode and triboelectric layer, which is 10 times higher than that of TENG without a charge storage layer [31]. Xu et al. created a charge pump to significantly improve the TENG's charge density, which can reach as high as 1020 $\mu C \cdot m^{-2}$ in ambient conditions [32]. Liu et al. used a charge excitation strategy to achieve an average surface charge density of 2.38 $mC \cdot m^{-2}$ for triboelectric materials, which is about 8 times higher compared to that using corona discharge [33]. However, simply enhancing the charge density will often lead to air breakdown and thus decrease the output performance of TENG. Therefore, a theoretical method is required to prevent air breakdown and reduce wasted energy caused by breakdown for practical application.

In this work, we reported a high-performance rotary triboelectric nanogenerator (R-TENG) based on a composited intermediate layer with highly oriented BTO nanoparticles to increase surface charge density and customize theoretical simulations to decrease the breakdown between a gradient electrode gap. The customized theoretical simulations based on the gradient electrode gap were established to optimize the competitive relationship between the gap area and the actual friction area, which can prevent air breakdown and enhance the output energy of R-TENG by at least 1.5 times. Compared to the traditional parallel interdigital electrode with the same gap distance, the air breakdown position between the gradient electrode gap will be easier to predict and is more likely to prevent air breakdown according to the customized theoretical model. Meanwhile, an intermediate layer which consists of barium titanate (BTO) and Polydimethylsiloxane (PDMS), was introduced to increase the surface charge density of the triboelectric layer but also increase the breakdown threshold, making it more difficult for breakdown to occur. Owing these

strategies, the open-circuit voltage can reach more than 6 kV with the help of a management circuit, and the short-circuit current density (J_{sc}) and transferred charge density (ΔQ_{sc}) can reach up to 4.2 $mA \cdot m^{-2}$ and 19.1 $\mu C \cdot m^{-2}$, respectively. The R-TENG can be utilized for powering up 3420 LEDs or 4 serially connected 36 W household fluorescent lamps continuously. In addition, a self-powered high-voltage disease prevention system is designed to reduce the risk of disease transmission. This work presents an important approach for guiding the further development of TENGs toward efficient energy harvesting and practical applications.

2　Results and discussion

A high-performance R-TENG is composed of two parts: a rotator and a stator. The structure and preparation processes of the high-performance TENG are shown in Fig. 1(a). Firstly, a layer of carbon nanotubes (CNTs) was coated by a blade on an acrylic substrate as an electrode matrix because CNTs have excellent electrical conductivity and mechanical properties (Fig. 1(a)-ii). Then a laser was used to cut out the shapes of the rotator and stator (Fig. 1(a)-iv). The electrodes of the stator are composed of two complementary-patterned grid electrodes with an alterable grid number and a variable interval angle. And the rotor was cut with only one grid pattern. Thirdly, a composite film was synthesized by mixing PDMS and ferroelectric BTO nanoparticles above the CNTs electrode layer of the stator (Fig. 1(a)-v). According to the previous reports [30, 34, 35], the intermediate layer of the PDMS/BTO can enhance the performance of TENG due to the ferroelectricity and high permittivity of BTO nanoparticles. The mechanism of the intermediate layer will be thoroughly elaborated in Fig. S11 in the Electronic Supplementary Materials (ESM). Then, the nanocomposite film was treated with a high-voltage field to polarize the BTO nanoparticles. Finally, a fluorinated ethylene propylene (FEP) film as a negative electrification layer was attached to the PDMS/BTO nanocomposite film of the TENG's stator. At the same time, a Polyamide6 (PA6) film as a positive electrification layer and a foam tape buffer layer were pasted on the rotor of the TENG. The existence of the foam layer can enhance the friction sufficiently and thus significantly improve the output performance of the R-TENG. The detailed preparation process of R-TENG is presented in the methods section.

A scanning electron microscope was used to characterize the morphology of the CNTs electrode and the BTO nanoparticles. The agglomerated distribution of CNTs contributes to a large number of nanocavities in the CNTs layer, as shown in Fig. 1(b). The cross-linked CNTs network is the crucial factor for high conductivity. A high-resolution image of a single CNT nanowire is shown in Fig. 1(c). The SEM image demonstrates that the average nanoparticle size of ferroelectric BTO is about 100 nm, and XRD was used to clarify the crystal structure of BTO nanoparticles further, as shown in Figs. 1(d) and 1(e). The main diffraction peaks of BTO
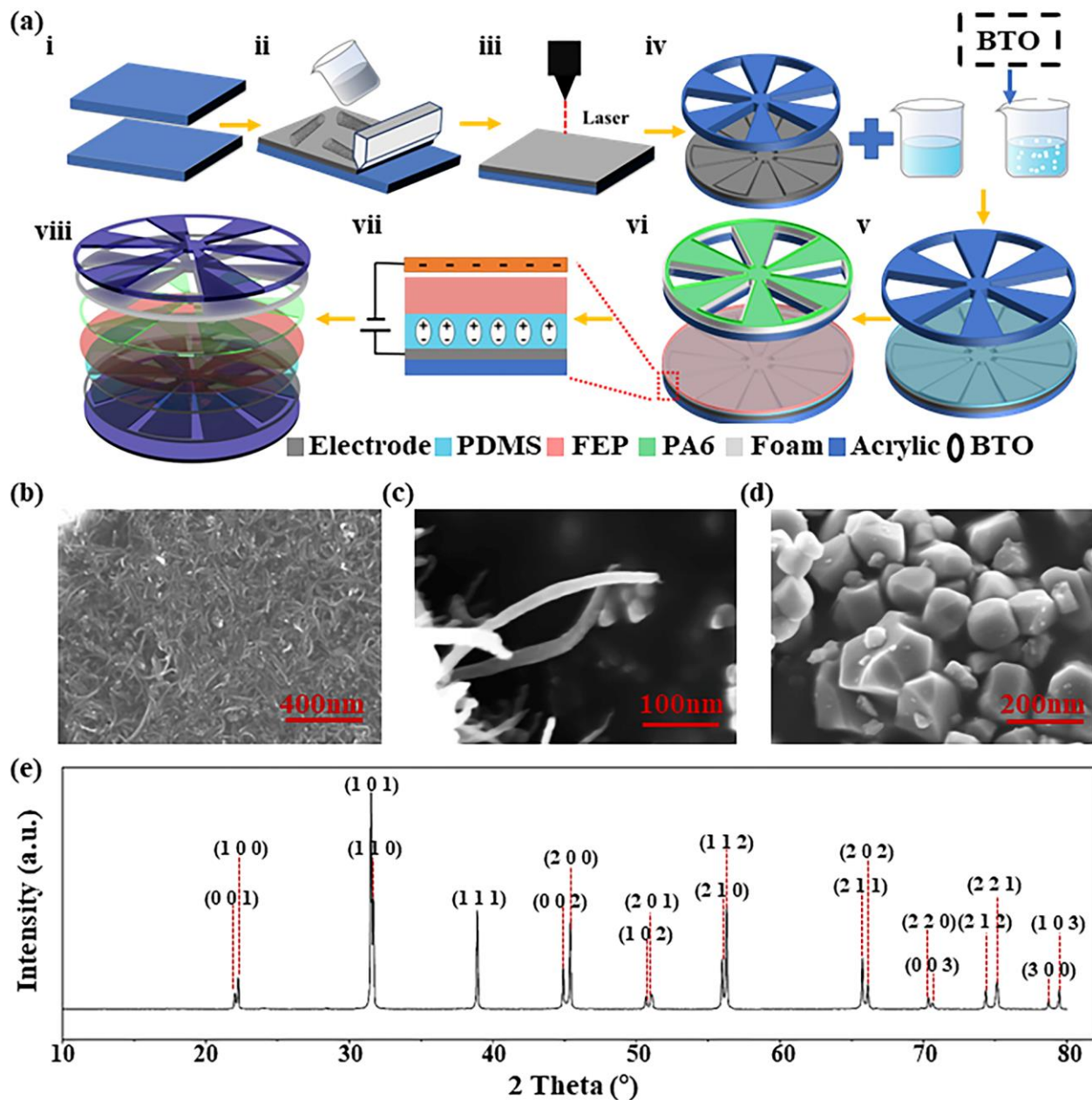
Figure 1 (a) Schematic diagram of the high-performance R-TENG structure and manufacturing process. (b) The surface morphology of CNTs electrode. (c) The surface morphology of a single CNT nanowire. (d) The surface morphology of ferroelectric BTO nanoparticles by using SEM. (e) XRD pattern of ferroelectric BTO nanoparticles.

primarily appear at 2θ of 31.50°, 31.68°, and 45.41°. And the two peaks around 45°, which are well recognized and indexed to (002) and (200), revealed that the crystal structure of ferroelectric BTO nanoparticles is the tetragonal phase, which is consistent with the morphology of the SEM result. The schematic diagram of the tetragonal BTO crystal structure is shown in Fig. S1 in the ESM.

According to previous research [36, 37], the breakdown effect universally occurs in the practical application of various TENGs, and the output energy of TENG is seriously limited by the breakdown effect. This is because the air breakdown effect causes the charges generated at the surface of TENG to diffuse into the atmosphere, resulting in charge loss and a decrease in surface charge density [38]. Hence, how to avoid air breakdown

becomes the key to improving the performance of TENG. Although the breakdown effects of contact-separation (CS) TENG and traditional sliding freestanding (SFT) TENG with a certain electrode gap have already been studied. But the breakdown effect of the rotation SFT-TENG with the gradient gap between the electrodes still needs to be modified. Two points need to be clarified when considering this rotary SFT-TENG. Firstly, there is a competitive relationship between the gap area and the actual friction area. When the gap angle (θ_g) increases, as shown in Fig. 2(a), the actual friction area will decrease. Increasing the θ_g will enlarge the breakdown threshold and thus decrease the air breakdown, enhancing the output performance of the R-TENG. However, the decreasing of the actual friction area will reduce the total amount of the

triboelectric charges, weakening the output performance of the R-TENG. This phenomenon does not exist in traditional sliding freestanding (SFT) TENG (shown in Fig. S2 in the ESM) because we can increase the gap distance without decreasing the friction area). Therefore, the competitive relationship between the gap area and the actual friction area requires a customized theoretical model to optimize the R-TENG output.

Secondly, the air breakdown position between the gradient electrode gap of R-TENG will be easier to predict when compared to the traditional SFT-TENG with the same gap distance of the parallel interdigital electrodes. Therefore, a customized theoretical model should be established to provide the optimized gap angle (θ_g) and optimized segment number of grid electrodes (N).
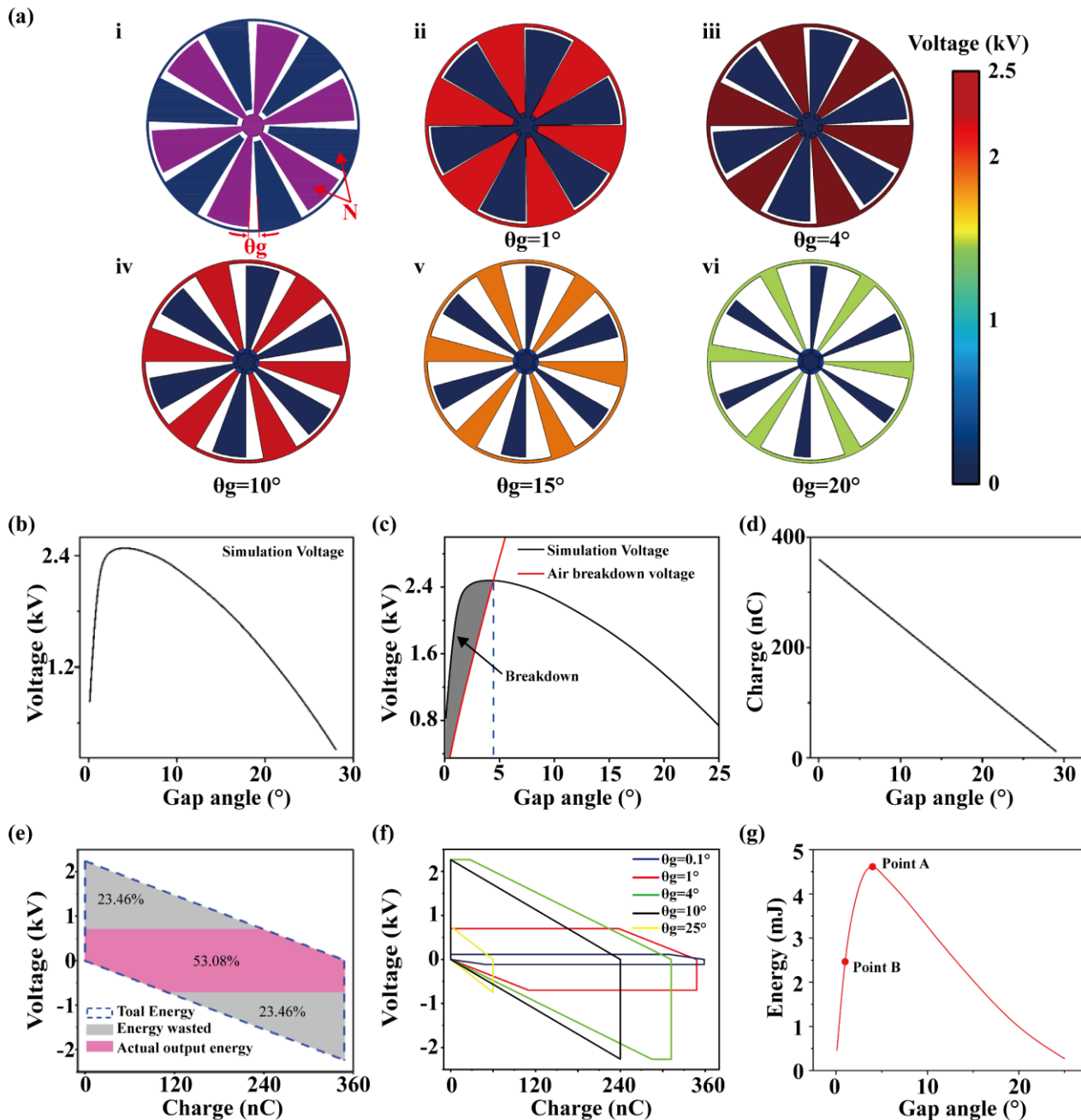

Figure 2 (a) Simulated potential distribution of R-TENGs under different gap angles θ_g (θ_g = (ii) 1.0°, (iii) 4°, (iv) 10.0°, (v) 15.0°, and (vi) 20.0°). (b) The simulation voltage V_s with different θ_g. (c) The relationship between the simulation voltage and the breakdown voltage V_b. (d) The transferred charge with θ_g. (e) The V–Q plot with air breakdown when θ_g is 1.0°. (f) The V–Q plot of different θ_g with air breakdown. (g) The actual output energy of R-TENG with different θ_g

As shown in Fig. 2, there exists the best gap angle to ensure the largest output energy of the R-TENG. In Fig. 2(a)-i, the gap angle between each gate electrode unit is defined as θ_g. The segment number of the grid electrode is defined as N. The finite element method is used to explore the relationship between θ_g

and output voltage/energy when N is fixed at 6. The materials and parameters used in the COMSOL simulation are listed in Supplementary Table S1. Due to the gradient gap between two electrodes, the minimum distance (d_{min}) affects the magnitude of the air breakdown voltage, shown in Eq. (1). And the

breakdown voltage (V_b) can be calculated directly by Paschen's law [37], as shown in Eq. (2).

$$d_{\text{mim}} = R_2 \times \sin \theta_g \qquad (1)$$

$$V_b = \frac{B\rho d}{\ln A\rho d - \ln\left(\ln\left(1 + \frac{1}{\gamma_{se}}\right)\right)} \qquad (2)$$

Herein, p is the operating pressure, and d is the distance between two gate electrode units. A, B, and γ_{se} are constants related to the excitation-ionization energies, the saturation ionization, and the gas composition, respectively.

Meanwhile, the simulated voltages (V_s) by the finite element method, which means the potential difference between two electrodes, are presented in Fig. 2(a) ii-vi. The total simulated voltages with different gap angles are plotted in Fig. 2(b). The curve of the breakdown voltage threshold calculated by Eq. (2) is plotted in Fig. 2(c), which is marked with a red line. It is worth noting that there is a crossing point (θ_g is about 4°) when the calculated breakdown voltage threshold and the simulated voltage curve by COMSOL are equal. Therefore, when the θ_g is less than 4°, the air breakdown phenomenon will occur between the electrodes, causing the final output voltage to be limited by the calculated breakdown voltage, as shown in the red region in Fig. 2(c). And when the θ_g is larger than 4°, the final output voltage is not affected by the breakdown voltage. Thus, there is an optimal θ_g to maximize the actual output voltage value of the R-TENG.

However, the output energy of the R-TENG is not only affected by the actual output voltage but is also influenced by the transferred charges, which are related to the friction area. R_1 and R_2 represent the internal and external radii, as shown in Fig. S3 in the Supplementary Materials. And the friction area S_f can be defined as Eq. (3).

$$S_f = \frac{Q}{\sigma} = \left(1 - \frac{\theta_g}{360}N\right)\pi\left(R_2^2 - R_1^2\right) \qquad (1 \leq N) \quad (3)$$

It is obvious that the transferred charges or the friction area of the R-TENG decrease when the gap angle increases, as shown in Fig. 2(d). Since the actual output voltage first increases and then decreases, and the transferred charge decreases as the gap angle increase. Therefore, the actual output energy of the R-TENG, defined by the inner area of the V-Q curve [39], is quite complicated. The V-Q curve when θ_g is 1.0° is demonstrated to reveal the actual output energy of R-TENG (Fig. 2(e)). The simulated voltage V_s is about 2.2 kV, and the transferred charge is 360 nC. The area of the V-Q curve presents the maximum output energy in the theoretical situation without breakdown (the total area of the dashed parallelogram, Fig. 2(e)). And the actual output energy (pink area) will be much smaller due to the simulated voltage being larger than the air breakdown voltage. The energy wasted by the breakdown (the gray area) is up to about 46.92%, and the actual output energy is only 53.08% when $\theta_g = 1°$. Thus, it is quite important to choose the right θ_g and to restrict the breakdown. More V-Q curves modified by air breakdown voltage with different θ_g are plotted in Fig. 2(f). And the actual output energy of TENG (the area of the

modified Q-V curves) with different θ_g is plotted in Fig. 2(f). And the maximal actual output energy of 4.61 mJ (point A) can be achieved when θ_g is around 4°, which is about 1.5 times larger than that of point B (θ_g is 1.0°).

The segment number of gate electrode (N) is another vital structural parameter to influence the output performance of the R-TENG. Because the number of gate electrode units affects the contact area between the upper and lower triboelectric layer by determining the number of triboelectric units in the R-TENG rotor section. As shown in Fig. 3(a), the simulations of high-performance R-TENGs with different N are simulated when the θ_g is fixed. Although the optimized gap angle of the R-TENG is about 4° (when N is fixed as 6) according to the simulation results of Fig. 2, the friction area has a significant reduction, according to Eq. (3). The optimized gap angle will lead to a lot of wasted area when N becomes larger and larger. For example, when the $N = 18$, the total gap angle is $N \times \theta_g \times 2 = 144°$, which means the friction area only occupies about 216° with a proportion of 60%. Therefore, the θ_g is fixed at a small angle. The simulation results show that the output simulation voltage of R-TENG decreases with the increase of N, as shown in Fig. 3(b). According to the results, the maximal V_s is 3707 V when the N is 2, while it declines to about 1000 V when N is 18. The V_s shows a downward trend. The relationship between N and the amount of transferred charge in one output period, defined as Q_1, is plotted in Fig. 3(c). Due to the fixed gap angle, the friction area of the whole device will decrease when N increases, leading to a small decline in Q_1. However, when $N < 180 \div \theta_g$, the total transferred charges per cycle Q_2 (Defined as Q_1 multiplied by N.) increases expeditiously in Fig. 3(d) and Eq. (4), which shows the opposite trend of that of Q_1.

$$Q_2 = Q_1 N = \left(N - \frac{\theta_g}{360}N^2\right)\pi(R_2^2 - R_1^2)\sigma \qquad (4)$$

Therefore, the introduction of more gates in the structure will effectively improve the output frequency of the R-TENG. Similarly, the total output energy per cycle or segment output period can be calculated by the V-Q curve under the different N plotted in Fig. 3(e). The output energy per cycle almost increases rapidly at first ($N < 6$) and then becomes almost stable ($6 < N < 20$). Finally, the output energy per segment decreases when N is larger than 20 because both output voltage (Fig. 3(b)) and total transferred charges (Eq. (4)) decrease. Therefore, the optimized segment number of gate electrode N should be defined as 6, considering the largest energy output, the cost, and the difficulty of the fabrication.

The output performance of different structures of R-TENG is shown in Fig. S4 in the ESM. The results show that with the increase of the θ_g, the short-circuit current (I_{sc}) and transferred charges (Q_{sc}) are decreased when N is 3, as shown in Figs. S4(a) and S4(b) in the ESM. This is because the triboelectric area will be decreased with the increase of θ_g,
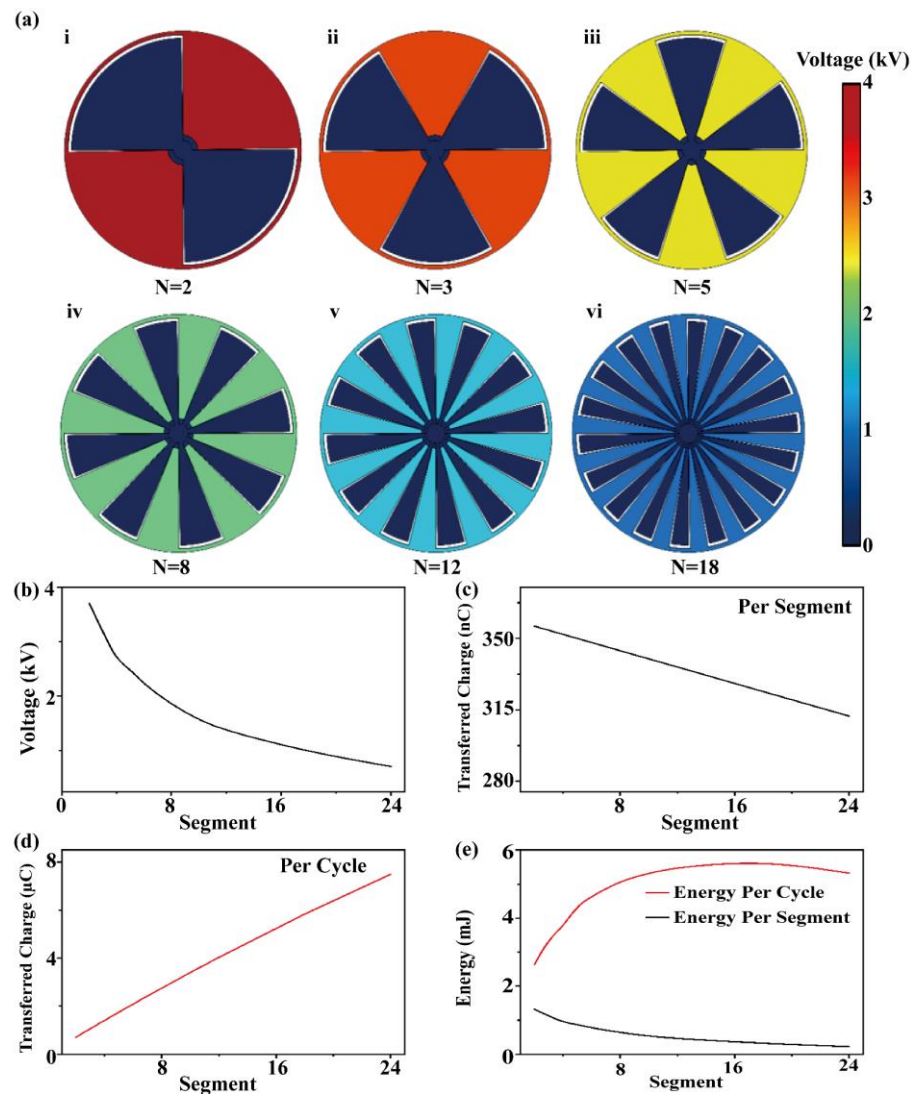
Figure 3 (a) Simulated potential distribution of R-TENGs under different segment numbers of electrode N (N = (i) 2, (ii) 3, (iii) 5, (iv) 8, (v) 12, (vi) 18). (b) The relationship between the simulation voltage and segment number. (c) The Q_1-N plot per segment. (d) The Q_2-N plot per cycle ($Q_2 = Q_2 \times N$). (e) The E-N plot per segment and per cycle

causing the decrease of the performance of the R-TENG. The I_{sc} and Q_{sc} can reach up to 4.2 µA and 160 nC when the θ_g is 4°, and N is 3. And the relationship between the performance of R-TENG and N is shown in Figs. S4(c) and S4(d) in the ESM. The I_{sc} of R-TENG is increased with the increase of N. When N is 6, the I_{sc} is maximum, which can reach 5.1 µA. This is due to the increase of N, which increases the frequency of the current of the R-TENG. However, the per-segment transferred charge is decreased with the increase of N. This is because the triboelectric area is decreased, leading to a decrease in transferred charges. And as the increased of N, the per-segment transferred charge decreased from 168 to 102 nC. And the per-cycle transferred charge is increased from 168 nC to 612 nC, As shown in Fig. S4(e) in the ESM. The results show that the I_{sc} of R-TENG is best when θ_g is 4°, and N is 6, corresponding to the simulation results.

Most previous research works only focus on the relationship of V–θ_g, V–N or Q–θ_g, Q–N. However, the voltage and transferred charges have different trends with θ_g and N, causing

the output energy (the inner area of the V–Q curve) that has not been well studied. Considering the optimized output energy and the breakdown between the gradient gap, the customized theoretical simulations take a huge step forward in TENGs applications.

Besides the customized theoretical simulations, an intermediate layer consisting of BTO and PDMS is introduced between the triboelectric layer and the electrodes layer to improve the output performance of the R-TENG further.

Figure 4(a) shows the basic operating mechanism of current generated by the high-performance R-TENG in the short-circuit condition. In the initial state (Fig. 4(a)-i), the PA6 film of the rotator and the FEP membrane above electrode I of the stator is at an entirely overlapping position, and there are negative charges on the surface of FEP while positive charges on the surface of PA6. The surface charge density of PA6 film is two times that of FEP film, which induces negative charges on the bottom electrode I and positive charges on the bottom electrode II to make the charges equilibrium. As the rotary is

rotating before it completely overlaps electrode II (Fig. 4(a)-ii), free charges will be redistributed between the electrodes, causing the positive charges to be transferred from electrode II to electrode I through external loads to generate a current. And then, in the following process from Fig. 4(a)-iii to Fig. 4(a)-iv, the rotary will rotate again to the original position (Fig. 4(a)-i), and positive charges will be transferred from electrode I back to electrode II, causing a reversed current. The sketch figures and finite element simulation by COMSOL are utilized to demonstrate the open-circuit voltage, as shown in Fig. 4(b). In the original state (Fig. 4(b)-i), there is no voltage difference between electrode I and II. As the rotary is rotating before it completely overlaps electrode II (Fig. 4(b)-ii), there is no charge transfer between the two electrodes due to the open-circuit circumstance. Thus, the voltage potential of electrode II will be much higher than that of electrode I. The voltage potential of electrode II can reach about 2000 V. When the rotary completely overlaps electrode I (Fig. 4(b)-iv), the voltage potential of electrode II is about -3000 V. The simulation results are consistent with the experimental results, as shown in Fig. 4(c). The maximum open-circuit voltage (V_{oc}) of the R-TENG can reach up to 2 kV.

The R-TENG is driven by a programmable rotary motor to obtain a determined speed, e.g., 120 rpm. The N is 6, and the θ_g between each unit is 4°. The experimental voltage of R-TENG is measured by using the voltage divider method, with two resistors with resistance values of 100 MΩ (R_1) and 100 GΩ (R_2) connected in series in the external circuit to simulate the open-circuit condition and increase the accuracy of measurement (Fig. S5 in the Supplementary Materials). The potential of electric I/II can reach more than 2 kV, and the potential difference between electrode I and electrode II can be as high as 5.5 kV. And the accuracy of open-circuit voltage generated by R-TENG is estimated by calculating the number of LEDs powered by the R-TENG. The short-circuit current density (J_{sc}) of the R-TENG can reach 4.2 mA·m^{-2} with a stable and continuous AC signal (Fig. 4(d) and Fig. S6(a) in the ESM). And the transferred charge density (ΔQ_{sc}) can reach up to 19.1 μC·m^{-2} at a peak-to-peak value at the same rotational speed (Fig. 4(e) and Fig. S6(c) in the ESM). The output power is equivalent to the Joule heating of the load resistor, calculated as $I^2 \times R$, where I is the current amplitude value under different load resistance, and R is the load resistance. At the matched load of 100 MΩ, the output power density can reach 18.6 W·m^{-2}, as shown in Fig. S7 in the ESM. Figure S8 in the ESM shows the stability of the R-TENG. The result shows that the short-circuit current density of the R-TENG can maintain about 4 mA·m^{-2} after 1 day's working (4 hours per day). And the current density can reach up to 3.83 mA·m^{-2} after 3 days of working. The short-circuit current density is reduced by 8.8% compared to the initial short-circuit current density of 4.2 mA·m^{-2}. Although the output of the TENG decreases after 7 days of working, the current density remains at about 3 mA·m^{-2}, which is still considerable. Figure S9 in the ESM shows the surface morphology of the triboelectric layer of the active layer. Although there are many scratches on the surface captured by the microscope after 7 days of working (4 hours per day), the surface morphology of the triboelectric layer did not show a significant difference from the initial state. And the output performances are still considerable, demonstrating that the R-TENG has good operational stability.

It should be emphasized that the high-performance R-TENG can even be directly utilized for driving 2 serially connected 36 W fluorescent lamps (Fig. 4(f) and Movie ESM1). As shown in Fig. 4(g) and Movie ESM2, the high-performance R-TENG can light up more than 1160 serially connected LEDs without any management circuit. This result demonstrates that the sustainable output voltage of the R-TENG is at least more than 2 kV.

The R-TENG could convert the collected low-frequency mechanical energy (such as wind energy) into electrical energy to drive wireless transmission equipment [40, 41] (Fig. 4(h)). Furthermore, a high-performance wireless transmission system based on the high-performance R-TENG is fabricated to explore the wireless application of the TENGs. As shown in Fig. S10(a) in the ESM, the wireless transmission system is composed of five parts: the high-performance R-TENG is used to harvest the mechanical energy, a rectifier to convert AC to DC, a capacitor for storing energy, a wireless transmitter, and a receiver. The energy generated by the TENG is stored by the capacitor. Then the wireless transmitter is powered by the capacitor and emits 8-byte signals to the wireless receiver, and the signal could be set as "ashining". Next, the wireless receiver linked to the computer can receive the signal. And Fig. S10(b) in the ESM shows that the R-TENG can charge a 10-mF capacitor from 0 to 5 V in about 35 min by harvesting the mechanical energy and then operating the wireless transmitter. The voltage of the capacitor rapidly descends to about 2.0 V as the wireless transmitter emits 8-byte signals. To demonstrate the effectiveness of the R-TENG-based wireless transmission, the performance of the system was tested at different distances. As shown in Fig. 4(i), when a distance of 10 m separates the transmitter and receiver, the receiver can receive very distinct 8-byte signals 4 times. And the performance of the wireless transmission system with different distances can be seen in Fig. S10(c) in the ESM. It is worth noting that the receiver can still receive a stable 8-byte signal 4 times when the distance increases from 1 m (Fig. S10(c)-I in the ESM) to 50 m (Fig. S10(c)-iii in the ESM and Movie ESM3). The results show that the R-TENG-based wireless transmission system has excellent performance. According to the previous reports, these results are among the best-performing triboelectric generators.

Previous research pointed out that the intermediate layer can enhance the output performance of a TENG by these two major methods [42–44]. Firstly, the intermediate
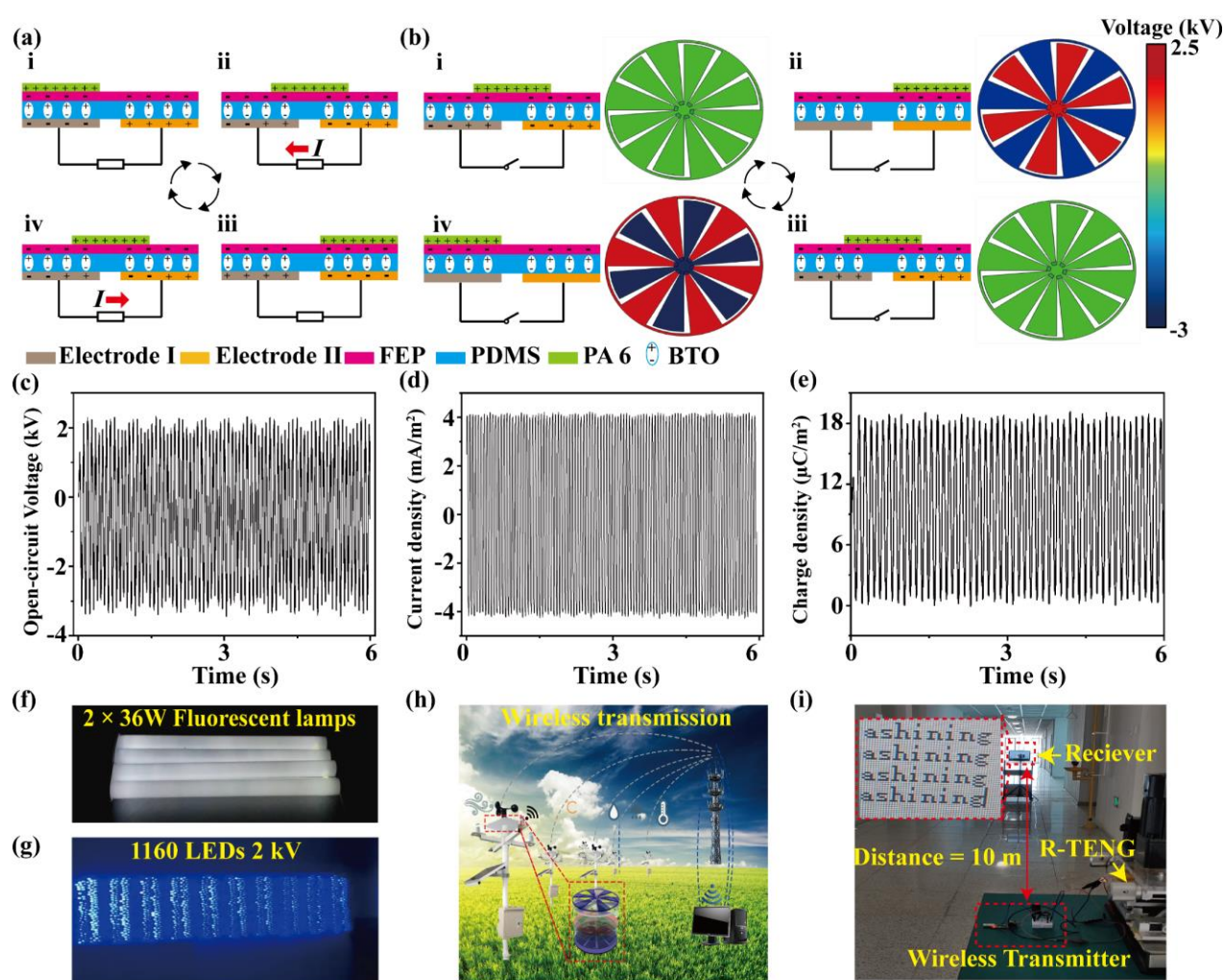
Figure 4 (a) Illustrates the working mechanism in the short-circuit condition. (b) Schematic illustration of the working mechanism in the open-circuit condition and the COMSOL simulation. (c) Open-circuit Voltage V_{OC}. (d) Short-circuit current density J_{SC}. (e) Short-circuit transferred charge density ΔQ_{SC} of the high-performance R-TENG. (f) Two 36 W household fluorescent lamps lighted directly by the R-TENG. (g) 1160 LEDs lighted directly by the R-TENG. (h) Schematic illustration of wireless transmission application of the R-TENG for wind energy harvesting. (i) The performance of the wireless transmission system with a distance of 10 m. The inset image shows the signal received by the wireless receiver.

layer contains deep traps with large trap density, which can effectively trap and retain triboelectric charges, resulting in enhanced performance of the TENGs. Secondly, the high dielectric constant of the intermediate layer will inhibit the recombination of negative charges from the friction layer and positive charges from electrodes, causing the breakdown or leakage current more difficult.

Although researchers have studied the impact of the high dielectric constant BTO nanoparticles in TENG [45, 46], many added BTO nanoparticles into the friction layer, revealing that the ferroelectric nanocomposites will enhance the contact-electrification effect of the friction layer. Others simply added the BTO nanoparticles into the intermediate layer without any treatment. Therefore, the inner dipoles of BTO nanoparticles are mostly disordered, as shown in Fig. S11(b) in the ESM, which will cancel each other and have little influence on the friction layer. Thus, the highly oriented inner dipoles of BTO nanoparticles should be fabricated.

The highly oriented dipoles in ferroelectric BTO domains can be obtained by applying an external electric field [47–49]. After 2 hours of polarization, the inner dipoles of BTO nanoparticles will be oriented under the action of the external electric field, as shown in Fig. S11(c) in the ESM. And the polarized PDMS/BTO nanocomposite film is introduced into the TENG device as the intermediate layer between the FEP triboelectric layer and the CNTs electrode layer (Fig. S11(d) in the ESM). Therefore, an extra inner electric field will be formed between the positive dipoles of BTO nanoparticles and the negative triboelectric charges of the FEP friction layer. Due to the affection of the extra inner electric field, which has been studied in many fields [50, 51], the triboelectric charges of the FEP surface are difficult to escape, which will considerably improve the retention ability of the triboelectric charges and increase the outputs of the TENG, as shown in Fig. S11(d) in the ESM. To verify the role of the highly oriented BTO nanoparticle intermediate layer, we compared the output performances of three different FST-TENGs: without intermediate layer, with unpolarized PDMS/BTO intermediate

layer, and with highly oriented PDMS/BTO intermediate layer. A programmable linear motor was used to drive the FST-TENG at 0.4 Hz. As shown in Figs. S11(e) and S11(f) in the ESM, both the short-circuit current and open-circuit voltage of the TENG with highly oriented PDMS/BTO intermediate layer are the highest, which are 2.5 times and 2 times as the FST-TENG without intermediate layer respectively. And different voltages are applied to polarize the BTO, and the performances of different voltage-polarized BTO intermediate layers are shown in Fig. S12 in the ESM. It is obvious that the performance increases with the polarization voltage, which means the orientation of the BTO is improved. The residual polarization intensities are also measured, as shown in Fig. S13 in the ESM. As the polarization electric field increases, the residual polarization intensity (P_r) and maximum polarization intensity (P_{max}) are increased, leading to an increase in the degree of the ordering of the BTO dipole [52]. When the electric field increased from 0.5 to 4 MV·cm^{-1}, the P_r increased from 0.04 to 0.59 μC·cm^{-2}, which increased 14.75 times. And the P_{max} increases to 2.4 μC·cm^{-2}, which is 7.5 times higher than that of the electric field is 0.5 MV·cm^{-1}. These results provide strong evidence that the orientation of BTO is improved and that adding an oriented BTO nanocomposite intermediate layer can significantly enhance the performance of TENG. And according to the related research [48], the output performance of TENG increases and then decreases with the increase in BTO concentration. When the BTO concentration is too high, the BTO NPs will agglomerate in the matrix, forming a leakage current path and making it easier for air breakdown to occur [53]. The output performance of FST-TENG was optimal when the BTO concentration was 20%. Owning these strategies, the high-performance rotary triboelectric nanogenerator (R-TENG) is fabricated. The composited intermediate layer with highly oriented BTO nanoparticles is designed to increase surface charge density and the retention ability of the triboelectric charges. Meanwhile, customized theoretical simulations are developed to decrease the breakdown between a gradient electrode gap. Thus, the high-performance R-TENG is one of the best-performing triboelectric generators so far.

A management circuit (MC) is also designed to enhance the output voltage of the TENG to meet the demands of commercial applications. High-voltage power sources have various applications in our daily life, such as electrostatic generators [54], electrospinning [55], and so on. Although the output voltage (V_{out}) of the R-TENG is more than 2 kV, it is still a bit lower when applied to some high-voltage devices, such as electronic mosquito swatters. Therefore, a management circuit is designed to improve the output voltage of the high-performance R-TENG. The working mechanisms of the voltage multiplier circuit are shown in Fig. S14 in the ESM. The working principle of the management circuit is similar to that of the rectifier bridge, which is consisted of capacitors and

diodes. The rectifier bridge will generate only positive signals. Under the first positive cycle, the voltage on C1 (V_{C1}) is equal to the output voltage of the TENG, with the negative on the left and the positive on the right (Fig. S14(a) in the ESM). For the double voltage circuit, when the TENG current is in the negative periodic (Fig. S14(b) in the ESM), D1 is in a reverse blocking state, while D2 is in the forward conducting state. The current flows through D2 to charge the capacitor C2. Based on Kirchhoff voltage laws (KVL), V_{C2} is doubled compared with V_{TENG}, with the cathode on the left and the anode on the opposite side. Similarly, when the TENG current is in the positive periodic (Fig. S14(c) in the ESM), D2 is in a reverse blocking state, which acts like a turned-off switch. Therefore, the polarity of the voltage of C2 does not change, which remains negative on the left and positive on the right. As the output voltage V_{out} equals V_{C2}, the output voltage is always positive. Similarly, for the triple voltage circuit, C3 is charged to V_{C3} (Fig. S14(d) in the ESM). And $V_{C1} = V_{TENG}$, $V_{C2} = 2V_{TENG}$ and $V_{C3} = 2V_{TENG}$. Therefore, the final output voltage V_{out} is the sum of V_{C1} and V_{C3}, 3 times as big as V_{TENG}. And the output voltage is always positive.

Figure 5(a) shows the V_{out} of the R-TENG without the MC, which demonstrates that the maximum output voltage is about 2 kV. And the output voltage of the R-TENG could be enhanced about 2 and 3 times when connected to the MCs, reaching the maximum V_{out} as high as 4 kV (Fig. 5(b)) and 6 kV (Fig. 5(c)), respectively. With the triple voltage multiplier circuit, the high-performance R-TENG can light up 3420 serially connected LEDs, demonstrating that the sustainable output voltage of R-TENG is at least more than 6 kV, as shown in Fig. 5(d) and Movie ESM4. In addition, it can be utilized for powering up 4 serially connected 36 W fluorescent lamps continuously, as shown in Fig. 5(e) and Movie ESM5. These results reveal that the MC system plays an important role in improving the outputs of the R-TENG. Since the voltage is amplified to at least 6 kV and the current is still as low as several microamperes when harvesting the wind energy, which is quite powerful and safe to drive the electronic mosquito swatter. As shown in Fig. S15 in the ESM, the self-powered high-voltage disease prevention system is composed of a high-performance R-TENG as a high-voltage power source, an MC system as a voltage amplifier, and electrodes withdrawn from a household electronic mosquito swatter. The potential distribution between the two grid electrodes of electronic mosquito swatter is simulated by COMSOL software, as shown in Fig. 5(f) and Fig. S16 in the ESM. And it is obvious to observe the sparks between the net electrodes when the high-performance R-TENG powers the electrodes withdrew from the mosquito swatter, as shown in Fig. S17 in the ESM. These results provide the possibility of using the high-performance R-TENG with an MC system to kill mosquitoes. Figure S18 in the ESM shows the process of killing a mosquito with an obvious spark when a
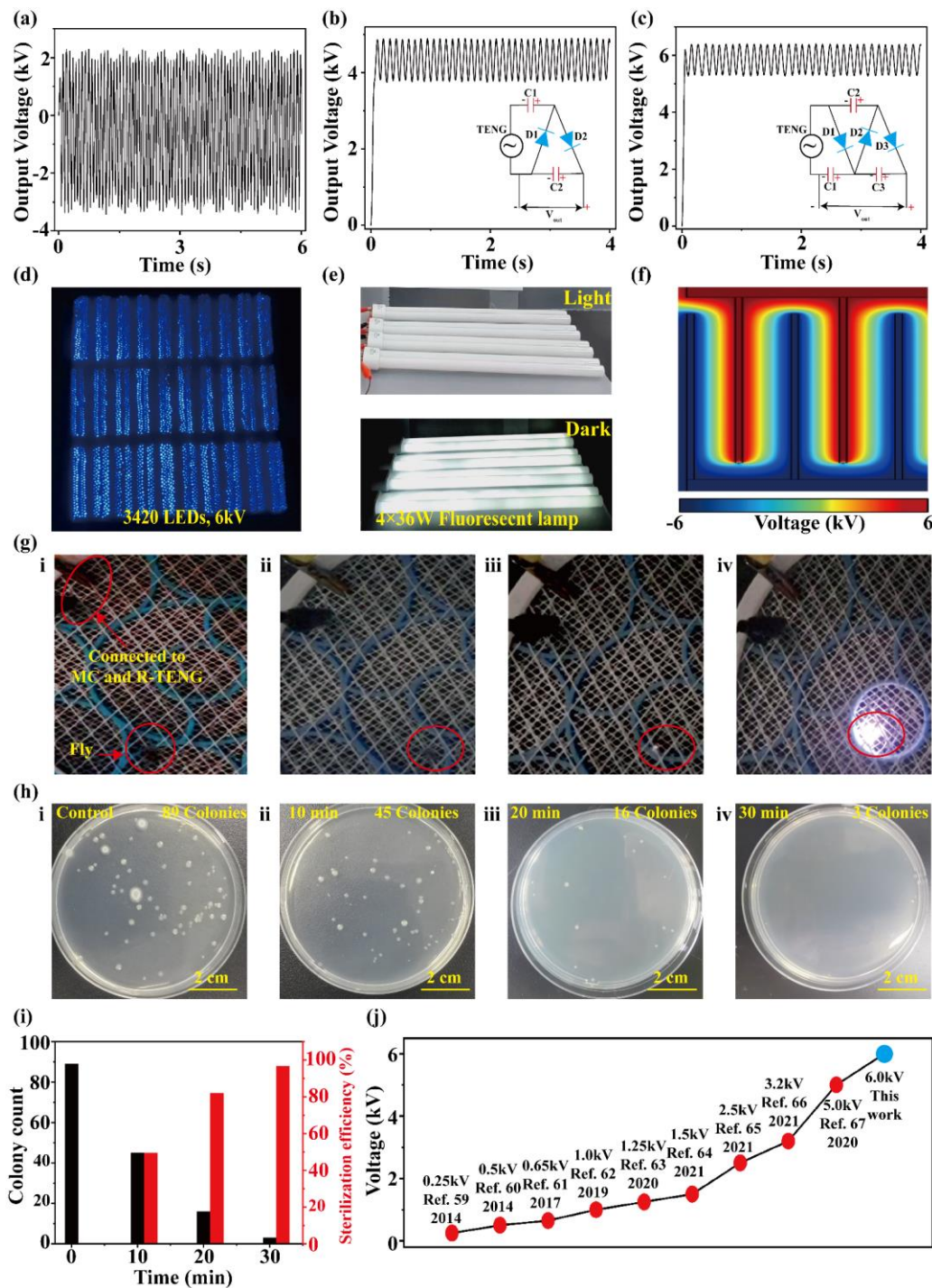
Figure 5 The output voltage (V_{out})of R-TENG (a) without the management circuit (MC), (b) with a double voltage multiplier circuit (The inset diagram shows the circuit of the double voltage multiplier), and (c) with a triple voltage multiplier circuit (The inset diagram shows the circuit of the triple voltage multiplier). (d) 3420 LEDs lighted by the R-TENG with the MC. (e) Four 36 W household fluorescent lamps lighted by R-TENG with the MC. (f) The simulated potential distribution of the electrodes. (g) The process when the fly touches the electronic mosquito swatter powered by the R-TENG with MC. (h) Photographs of the colonies numbers under different sterilization times (i) 0 mim (ii)10 min (iii) 20 min (iv) 30 min. (i) The sterilization efficiency and colony counts under different sterilization times. (j) The voltage of this work is compared with those of other works.

mosquito contacts the electrodes. In addition, a much larger fly could also be killed by the self-powered high-voltage disease prevention system. Figure 5(g) shows the momentary situation of the fly before and after getting in touch with the grid electrodes, respectively. When the fly touches the grid

electrodes, it can be seen that a visible electric spark is produced. The complete fly-killing and mosquito-killing processes are captured by the high-speed camera, as shown in Movies ESM6 and ESM7, respectively. It should be emphasized that self-powered high-voltage disease prevention system is fairly safe for

humans due to its low current, which is much lower than the safe current. The researchers only have a slight stinging sensation when their fingers touch the electrodes unconsciously. The safe, high-performance self-powered high-voltage disease system is suitable for pest control, especially in isolated islands or remote/poor areas.

And the high-performance self-powered high-voltage disease prevention system also could achieve high-voltage sterilization. Due to differences in electrical properties between cell structures and liquid systems. When the liquid system is placed in a high-voltage electric field as a dielectric, the cell membrane of the microorganism in the liquid will be broken down by electricity under the action of a strong electric field, resulting in irreparable perforation or rupture, which will damage the cell tissue and lead to the inactivation of the microorganism [56–58]. The voltage of R-TENG can reach 6 kV with the help of the management circuit, so the R-TENG can be used to achieve high-efficiency sterilization. To demonstrate the sterilization effect of the self-powered high-voltage disease prevention system, the E. coil was treated under the high-voltage electric field generated by the R-TENG for 0–30 minutes, and the results of the sterilization are shown in Fig. 5(h). As the time of the sterilization increased, the colony numbers of the E. coil significantly reduced. After 30 minutes, there were only three colonies still alive. And the sterilization efficiency also could be calculated by counting the colonies from Fig. 5(h), as shown in Fig. 5(i). The results show that under the action of the high-voltage electric field generated by R-TENG for 30 min, the number of colonies was reduced from the initial 87 to 3, the survival rate of E. coil is about 3.45%, and the sterilization efficiency of the high-voltage disease prevention system can reach about 96.55%. These results show that the self-powered high-voltage disease prevention system performs well and provides a new strategy for protecting human health. And when compared with those similar TENGs from other research, as shown in Fig. 5(j), the output voltage of the R-TENG is much higher [59–67], and the R-TENG improved by the strategies mentioned before is among the best-performing triboelectric generators.

3   Conclusion

In summary, we developed a high-performance R-TENG by developing customized theoretical simulations to decrease the breakdown between a gradient electrode gap and a composited intermediate layer with highly oriented BTO nanoparticles to increase surface charge density. The customized theoretical simulations demonstrate that the rotary TENG will generate the highest output energy with the optimized gap angle of 4° and the segment number of grid electrode 6. The maximal actual output energy can be achieved about 1.5 times larger than that without air breakdown prevention. And an intermediate layer composed of highly oriented BTO nanoparticles is introduced further to enhance the charging density and the output performances. And a wireless transmission system is designed based on the high-performance R-TENG, which can still emit and receive the signal at a distance of 50 m. Furthermore, with the help of a

management circuit, the maximum output voltage of R-TENG can reach up to 6 kV, and it can light 3420 LEDs or 4 serially connected 36 W household fluorescent lamps. Based on its excellent performance, the self-powered high-voltage disease prevention system was designed to decrease the transmission of diseases and guarantee public or individual health, which enriches the applications of TENGs and promotes the commercialization process.

4   Experiment section and methods

Materials. PDMS was purchased from Shenzhen Ausbond Co., LTD (Shenzhen, China). Carbon nanotube solution (9-10 wt%) was purchased from Shanghai Aladdin Biochemical Technology Co., Ltd (Shanghai, China). BTO nanoparticles were purchased from Shanghai Macklin Biochemical Co., Ltd (Shanghai, China). Polyamide 6 (PA6) film, fluorinated ethylene propylene (FEP) film, and acrylic were purchased from local stores.

Fabrication of the PDMS/BTO nanocomposite film. In this experiment, the PDMS solution is composed of the elastomer and the curing agent in a mass ratio of 10:1. The mass fraction of ferroelectric BTO nanoparticles is 20 wt.%. The preparation process of PDMS/BTO composite films is as follows, first, the ferroelectric BTO nanoparticles were mixed into the elastomer by ultrasonic dispersing for 30 min to ensure that the ferroelectric BTO nanoparticles were uniformly dispersed in the elastomer. Then, the curing agent was added to the mixture by stirring for 15 min to form a homogeneous mixture. Third, the mixture was evacuated at room temperature using a vacuum oven and kept at 293 K for 5 min to eliminate the air inside the mixture. Then, the mixture was poured into a template and placed at 293 K for 24 h to get cured. Finally, the PDMS-BTO composite film was separated from the template.

Fabrication of the CNTs electrodes. The electrodes are composed of CNTs. The bottom electrode is divided into two parts: inner and outer electrodes. Each part consists of 6 interconnected sector units with a central angle of 26°. The inner and outer radii of the inner electrodes are 15 mm and 90 mm. The inner and outer radii of the outer electrodes are 25 and 100 mm. First, the carbon nanotube solution was poured into the acrylic template and then kept in the oven at 323 K for 2 h to get cured. Third, a laser was used to cut the shape of the electrodes, respectively. Finally, the excessive carbon nanotubes were removed, leaving the electrode part. The thickness of CNTs electrodes is 50 μm.

Fabrication of the high-performance R-TENG. The diameter of the TENG is 200 mm. For the stator, firstly, FEP film (thickness, 30 μm), PA6 film (thickness, 50 μm), and PDMS/BTO nanocomposite film (thickness, 100 μm) were cleaned with ethanol and deionized water, respectively. Then, the PDMS/BTO nanocomposite film was attached to the CNTs electrodes using Kapton double-side tape. Third, the PDMS/BTO film of the stator was polarized under the effect of a negative electric field of 20 kV for 2 h. Finally, the FEP was attached to the PDMS/BTO nanocomposite film. And for the rotor consists of 6 interconnected sector units with a central angle of 26°. And the inner and outer radii are 15 and 100 mm.

Firstly, a laser was used to cut out the shape of the rotary on acrylic. Then, the double-sided foam tape was glued to the acrylic. Finally, the PA6 was attached to the foam layer.

Fabrication of the FST-TENG. The size of the FST-TENG is 60 mm × 60 mm. First, the CNTs electrodes (thickness, 50 μm) were cut into strips with a size of 60 mm × 25 mm by using a laser. The gap distance between the two electrodes is 10 mm. Then, the PDMS film (thickness, 100 μm) or polarized PDMS/BTO composite film (thickness, 100 μm) as an intermediate layer was attached to the top surface of CNTs electrodes. Finally, FEP was attached to the PDMS/BTO nanocomposite layer.

Characterization. The surface morphology of the BTO nanoparticles and CNTs was characterized by scanning electron microscopy (SEM, Carl Zeiss AG Gemini300). X-ray diffraction (XRD, Bruker Corporation (BRKR) d8 advance) was used to characterize the structure of BTO. The voltage was measured by using the voltage divider method. The voltage and transfer charge was measured by using an electrometer (Keithley 6514). The current was measured using a low-noise current preamplifier (Stanford research system, Model SR570). A motor (PERFECT, 5RK120RGU-CF) was used to drive the rotary of the high-performance TENG. A programmable linear motor (PERFECT, 57BYG250H-8) was used to drive FST-TENG. A high-voltage device (DONGWEN HIGH VOLTAGE, DW-N303-1ACH2) was used for polarizing the PDMS/BTO nanocomposite film.

Acknowledgements

The manuscript was written through the contributions of all authors. All authors have approved the final version of the manuscript.

Electronic Supplementary Material: Supplementary material (the simulation parameters set of different materials (Tables S1); the crystal structure of BaTiO₃; the performance of R-TENG with different θ_g and different N; the enlarged view output performance of the high-performance TENG; the stability of the R-TENG; the output performance of FST-TENG, the working mechanism of the voltage multiplier circuit; the schematic diagram of the self-powered mosquito-killing system and the mosquito-killing process; and the schematic diagrams and the images, including Movies ESM1–ESM7 and Figs. S1–S18) is available in the online version of this article at https://doi.org/10.26599/NRE.2023.9120074.

Declaration of conflicting interests

The authors declare no conflicting interests regarding the content of this article.

References

[1]   Cirimotich, C. M.; Dong, Y.; Clayton, A. M.; Sandiford, S. L.; Souza-Neto, J. A.; Mulenga, M.; Dimopoulos, G. Natural microbe-mediated refractoriness to Plasmodium infection in Anopheles gambiae. *Science* **2011**, *332*, 855-858.

[2]   Chan, M. Yellow fever: the resurgence of a forgotten disease. *Lancet* **2016**, *387*, 2165-2166.

[3]   Benelli, G.; Romano, D. Mosquito vectors of Zika virus. *Entomologia Generalis* **2017**, *36*, 309-318.

[4]   Song, L.; Zhou, B.; Zhu, H.; Duan, Q. Outdoor electric mosquito-killing apparatuses for malaria control in a hyperendemic area. *Clin. Infect Dis.* **2009**, *49*, 480.

[5]   Kim, K.-H.; Kabir, E.; Jahan, S. A. Exposure to pesticides and the associated human health effects. *Sci. Total Environ.* **2017**, *575*, 525-535.

[6]   Fan, F. R.; Tian, Z. Q.; Lin Wang, Z. Flexible triboelectric generator. *Nano Energy* **2012**, *1*, 328-334.

[7]   Wang, Z. L. On Maxwell's displacement current for energy and sensors: the origin of nanogenerators. *Mater. Today* **2017**, *20*, 74-82.

[8]   Wang, Z. L. On the first principle theory of nanogenerators from Maxwell's equations. *Nano Energy* **2020**, *68*, 104272.

[9]   Jin, L.; Zhang, B. b.; Zhang, L.; Yang, W. Q. Nanogenerator as new energy technology for self-powered intelligent transportation system. *Nano Energy* **2019**, *66*, 104086.

[10] Wu, Z. Y.; Cheng, T. H.; Wang, Z. L. Self-Powered Sensors and Systems Based on Nanogenerators. *Sensors (Basel)* **2020**, *20*, 2925.

[11] Pu, X.; Zhang, C.; Wang, Z. L. Triboelectric nanogenerators as wearable power sources and self-powered sensors. *Natl. Sci. Rev.* **2023**, *10*, nwac170.

[12] Liu, L.; Zhou, L.; Liu, D.; Yuan, W.; Chen, S.; Li, H.; Bian, Z.; Wang, J.; Wang, Z. L. Improved Degradation Efficiency of Levofloxacin by a Self-Powered Electrochemical System with Pulsed Direct-Current. *ACS Nano* **2021**, *15*, 5478-5485.

[13] Long, Y.; Yu, Y.; Yin, X.; Li, J.; Du, X.; Jiang, Y.; Wang, X. Effective anti-biofouling enabled by surface electric disturbance from water wave-driven nanogenerator. *Nano Energy* **2019**, *57*, 558-565.

[14] Luo, J. J.; Han, K.; Wu, X. Q.; Cai, H. H.; Jiang, T.; Zhou, H. B.; Wang, Z. L. Self-powered mobile sterilization and infection control system. *Nano Energy* **2021**, *88*, 106313.

[15] Zhao, T.; Xu, M.; Xiao, X.; Ma, Y.; Li, Z.; Wang, Z. L. Recent progress in blue energy harvesting for powering distributed sensors in ocean. *Nano Energy* **2021**, *88*, 106199.

[16] Yuan, Z. Q.; Wang, C. F.; Xi, J. G.; Han, X.; Li, J.; Han, S.-T.; Gao, W. C.; Pan, C. F. Spherical Triboelectric Nanogenerator with Dense Point Contacts for Harvesting Multidirectional Water Wave and Vibration Energy. *ACS Energy Lett.* **2021**, *6*, 2809-2816.

[17] Liang, X.; Jiang, T.; Liu, G. X.; Feng, Y. W.; Zhang, C.; Wang, Z. L. Spherical triboelectric nanogenerator integrated with power management module for harvesting multidirectional water wave energy. *Energy Environ. Sci.* **2020**, *13*, 277-285.

[18] Tang, S.; Chang, W. X.; Li, G.; Sun, J. F.; Du, Y.; Hui, X. D.; Tang, Q.; Hu, Z. H.; Li, J. Q.; Chen, J.; He, W. C.; Guo, H. Y. High performance wide frequency band triboelectric nanogenerator based on multilayer wave superstructure for harvesting vibration energy. *Nano Res.* **2023**, https://doi.org/10.1007/s12274-023-5476-6.

[19] Wang, S. H.; Xie, Y.; Niu, S. M.; Lin, L.; Liu, C.; Zhou, Y. S.; Wang, Z. L. Maximum surface charge density for triboelectric nanogenerators achieved by ionized-air injection: methodology and theoretical understanding. *Adv. Mater.* **2014**, *26*, 6720-6728.

[20] Li, S. Y.; Fan, Y.; Chen, H. Q.; Nie, J. H.; Liang, Y. X.; Tao, X. L.; Zhang, J.; Chen, X. Y.; Fu, E. g.; Wang, Z. L. Manipulating the triboelectric surface charge density of polymers by low-energy helium ion irradiation/implantation. *Energy Environ. Sci.* **2020**, *13*, 896-907.

[21] Fan, Y.; Li, S. Y.; Tao, X. L.; Wang, Y. F.; Liu, Z. Q.; Chen, H. Q.; Wu, Z. F.; Zhang, J.; Ren, F.; Chen, X. Y.; Fu, E. G. Negative triboelectric polymers with ultrahigh charge density induced by ion implantation. *Nano Energy* **2021**, *90*, 106574.

[22] Seung, W.; Yoon, H.-J.; Kim, T. Y.; Ryu, H.; Kim, J.; Lee, J.-H.; Lee, J. H.; Kim, S.; Park, Y. K.; Park, Y. J.; Kim, S.-W. Boosting Power-Generating Performance of Triboelectric Nanogenerators via Artificial Control of Ferroelectric Polarization and Dielectric Properties. *Adv. Energy Mater.* **2017**, *7*, 1600988.

[23] Liu, Y. H.; Mo, J. L.; Fu, Q.; Lu, Y. X.; Zhang, N.; Wang, S. F.; Nie, S. X. Enhancement of Triboelectric Charge Density by Chemical Functionalization. *Adv. Funct. Mater.* **2020**, *30*, 2004714.

[24] Wu, Y.; Wang, X. T.; Wang, Y. Q.; Nan, Y. B.; Xu, H.; Zhou, H.; Ren, M. P.; Duan, J. Z.; Huang, Y. L.; Hou, B. R. Enhancing the Performance of Triboelectric Nanogenerator Via Facile PDMS Surface Modification. *Adv. Eng. Mater.* **2023**, 2201442.

[25] Cheng, G.; Zheng, L.; Lin, Z. H.; Yang, J.; Du, Z. L.; Wang, Z. L. Multilayered⬜Electrode⬜Based Triboelectric Nanogenerators with Managed Output. *Adv. Energy Mater.* **2014**, *5*, 1401452.

[26] Chun, J. S.; Ye, B. U.; Lee, J. W.; Choi, D.; Kang, C. Y.; Kim, S. W.; Wang, Z. L.; Baik, J. M. Boosted output performance of triboelectric nanogenerator via electric double layer effect. *Nat. Commun.* **2016**, *7*, 12985.

[27] Jiang, T.; Pang, H.; An, J.; Lu, P. J.; Feng, Y. W.; Liang, X.; Zhong, W.; Wang, Z. L. Robust Swing⬜Structured Triboelectric Nanogenerator for Efficient Blue Energy Harvesting. *Adv. Energy Mater.* **2020**, *10*, 2000064.

[28] Bai, Y.; Xu, L.; Lin, S. Q.; Luo, J. J.; Qin, H. F.; Han, K.; Wang, Z. L. Charge Pumping Strategy for Rotation and Sliding Type Triboelectric Nanogenerators. *Adv. Energy Mater.* **2020**, *10*, 2000605.

[29] Li, G.; Fu, S. K.; Luo, C. Y.; Wang, P.; Du, Y.; Tang, Y. T.; Wang, Z.; He, W. C.; Liu, W. L.; Guo, H. Y.; Chen, J.; Hu, C. G. Constructing high output performance triboelectric nanogenerator via V-shape stack and self-charge excitation. *Nano Energy* **2022**, *96*.

[30] Jiang, H. X.; Lei, H.; Wen, Z.; Shi, J. H.; Bao, D. Q.; Chen, C.; Jiang, J. X.; Guan, Q. B.; Sun, X. H.; Lee, S. T. Charge-trapping-blocking layer for enhanced triboelectric nanogenerators. *Nano Energy* **2020**, *75*, 105011.

[31] Feng, Y.; Zheng, Y.; Zhang, G.; Wang, D.; Zhou, F.; Liu, W. A new protocol toward high output TENG with polyimide as charge storage layer. *Nano Energy* **2017**, *38*, 467-476.

[32] Xu, L.; Bu, T. Z.; Yang, X. D.; Zhang, C.; Wang, Z. L. Ultrahigh charge density realized by charge pumping at ambient conditions for triboelectric nanogenerators. *Nano Energy* **2018**, *49*, 625-633.

[33] Liu, Y.; Liu, W.; Wang, Z.; He, W.; Tang, Q.; Xi, Y.; Wang, X.; Guo, H.; Hu, C. Quantifying contact status and the air-breakdown model of charge-excitation triboelectric nanogenerators to maximize charge density. *Nat. Commun.* **2020**, *11*, 1599.

[34] Park, Y.; Shin, Y.-E.; Park, J.; Lee, Y. Ferroelectric Multilayer Nanocomposites with Polarization and Stress Concentration Structures for Enhanced Triboelectric Performances. *ACS Nano* **2020**, *14*, 7101-7110.

[35] Shin, S.-H.; Kim, Y.-H.; Lee, M. H.; Jung, J.-Y.; Nah, J. Hemispherically Aggregated BaTiO3 Nanoparticle Composite Thin Film for High-Performance Flexible Piezoelectric Nanogenerator. *ACS Nano* **2014**, *8*, 2766.Fu, J. J.; Xia, X.; Xu, G. Q.; Li, X. Y.; Zi, Y. L. On the Maximal Output Energy Density of Nanogenerators. *ACS Nano* **2019**, *13*, 13257-13263.

[36] Fu, J. J.; Xia, X.; Xu, G. Q.; Li, X. Y.; Zi, Y. L. On the Maximal Output Energy Density of Nanogenerators. *ACS Nano* **2019**, *13*, 13257-13263.

[37] Zi, Y. L.; Wu, C. S.; Ding, W. B.; Wang, Z. L. Maximized Effective Energy Output of Contact-Separation-Triggered Triboelectric Nanogenerators as Limited by Air Breakdown. *Adv. Funct. Mater.* **2017**, *27*, 1700049.

[38] Xie, X. K.; Chen, X. P.; Zhao, C.; Liu, Y. N.; Sun, X. h.; Zhao, C. Z.; Wen, Z. Intermediate layer for enhanced triboelectric nanogenerator. *Nano Energy* **2021**, *79*, 105439.

[39] Zi, Y. L.; Niu, S. M.; Wang, J.; Wen, Z.; Tang, W.; Wang, Z. L. Standards and figure-of-merits for quantifying the performance of triboelectric nanogenerators. *Nat. Commun.* **2015**, *6*, 8376.

[40] Fu, X. P.; Xu, S. H.; Gao, Y. Y.; Zhang, X. H.; Liu, G. X.; Zhou, H.; Lv, Y.; Zhang, C.; Wang, Z. L. Breeze-Wind-Energy-Powered Autonomous Wireless Anemometer Based on Rolling Contact-Electrification. *ACS Energy Lett.* **2021**, *6*, 2343-2350.

[41] Li, Y. H.; Yu, J.; Wei, Y. C.; Wang, Y. F.; Feng, Z. Y.; Cheng, L. Q.; Huo, Z. W.; Lei, Y. Q.; Sun, Q. Recent Progress in Self-Powered Wireless Sensors and Systems Based on TENG. *Sensors (Basel)* **2023**, *23*, s23031329.

[42] Wu, C. X.; Kim, T. W.; Park, J. H.; An, H. Q.; Shao, J. J.; Chen, X. Y.; Wang, Z. L. Enhanced Triboelectric Nanogenerators Based on MoS2 Monolayer Nanocomposites Acting as Electron-Acceptor Layers. *ACS Nano* **2017**, *11*, 8356-8363.

[43] Kim, D. W.; Lee, J. H.; You, I.; Kim, J. K.; Jeong, U. Adding a stretchable deep-trap interlayer for high-performance stretchable triboelectric nanogenerators. *Nano Energy* **2018**, *50*, 192-200.

[44] Firdous, I.; Fahim, M.; Daoud, W. A. Performance enhancement of triboelectric nanogenerator through hole and electron blocking layers-based interfacial design. *Nano Energy* **2021**, *82*, 105694.

[45] Tao, X. L.; Li, S. Y.; Shi, Y. X.; Wang, X. L.; Tian, J. W.; Liu, Z. Q.; Yang, P.; Chen, X. Y.; Wang, Z. L. Triboelectric Polymer with High Thermal Charge Stability for Harvesting Energy from 200 °C Flowing Air. *Adv. Funct. Mater.* **2021**, *31*, 2106082.

[46] Pandey, P.; Jung, D. H.; Choi, G. J.; Seo, M. K.; Lee, S.; Kim, J. M.; Park, I. K.; Sohn, J. I. Nafion-mediated barium titanate-polymer composite nanofibers-based triboelectric nanogenerator for self-powered smart street and home control system. *Nano Energy* **2023**, *107*, 108134.

[47] Shin, S.-H.; Kim, Y.-H.; Hyung, M.; Jung, L. J.-Y.; Nah, J. Hemispherically Aggregated BaTiO3 Nanoparticle Composite Thin Film for High-Performance Flexible Piezoelectric Nanogenerator. *ACS Nano* **2014**, *8*, 2766-2773.

[48] Suo, G. Q.; Yu, Y. H.; Zhang, Z. Y.; Wang, S. F.; Zhao, P.; Li, J. Y.; Wang, X. D. Piezoelectric and Triboelectric Dual Effects in Mechanical-Energy Harvesting Using BaTiO3/Polydimethylsiloxane Composite Film. *ACS Appl. Mater. Interfaces* **2016**, *8*, 34335-34341.

[49] Oh, H.; Kwak, S. S.; Kim, B.; Han, E.; Lim, G. H.; Kim, S. W.; Lim, B. Highly Conductive Ferroelectric Cellulose Composite Papers for Efficient Triboelectric Nanogenerators. *Adv. Funct. Mater.* **2019**, *29*, 1904066.

[50] Li, X. Y.; Chen, M. X.; Yu, R. M.; Zhang, T. P.; Song, D. S.; Liang, R. R.; Zhang, Q. L.; Cheng, S. B.; Dong, L.; Pan, A. L.; Wang, Z. L.; Zhu, J.; Pan, C. F. Enhancing Light Emission of ZnO-Nanofilm/Si-Micropillar Heterostructure Arrays by Piezo-Phototronic Effect. *Adv. Mater.* **2015**, *27*, 4447-4453.

[51] Ali, D.; Yu, B.; Duan, X. C.; Yu, H.; Zhu, M. F. Enhancement of output performance through post-poling technique on BaTiO3/PDMS-based triboelectric nanogenerator. *Nanotechnology* **2017**, *28*, 075203.

[52] Chai, B.; Shi, K. M.; Zou, H. Y.; Jiang, P. K.; Wu, Z. X.; Huang, X. Y. Conductive interlayer modulated ferroelectric nanocomposites for high performance triboelectric nanogenerator. *Nano Energy* **2022**, *91*, 106668.

[53] Li, Z. H.; Wang, X. L.; Hu, Y. Q.; Li, L. Z.; Wang, C. F. Triboelectric properties of BaTiO3/polyimide nanocomposite film. *Appl. Surf. Sci.* **2022**, *572*.

[54] Wang, J. Q.; Zi, Y. L.; Li, S. Y.; Chen, X. Y. High-voltage applications of the triboelectric nanogenerator—Opportunities brought by the unique energy technology. *MRS Energy & Sustainability* **2020**, *6*, e17.

[55] Li, C. J.; Yin, Y. Y.; Wang, B.; Zhou, T.; Wang, J. N.; Luo, J. J.; Tang, W.; Cao, R.; Yuan, Z. Q.; Li, N. W.; Du, X. Y.; Wang, C. R.; Zhao, S. Y.; Liu, Y. B.; Wang, Z. L. Self-Powered Electrospinning System Driven by a Triboelectric Nanogenerator. *ACS Nano* **2017**, *11*, 10439-10445.

[56] Cho, S. M.; Hanif, Z.; Yun, Y.; Khan, Z. A.; Jang, S.; Ra, Y.; Lin, Z.

H.; La, M.; Park, S. J.; Choi, D. Triboelectrification-driven microbial inactivation in a conductive cellulose filter for affordable, portable, and efficient water sterilization. *Nano Energy* **2021**, *88*, 106228.

[57]   Cai, C. C.; Luo, B.; Liu, T.; Gao, C.; Zhang, W. L.; Chi, M. C.; Meng, X. J.; Nie, S. X. Triboelectric pulsed direct current for self-powered sterilization of cellulose fiber. *Cellulose* **2022**, *29*, 7139-7149.

[58]   Tian, J. J.; Feng, H.; Yan, L.; Yu, M.; Ou Yang, H.; Li, H.; Jiang, W.; Jin, Y. M.; Zhu, G.; Li, Z.; Wang, Z. L. A self-powered sterilization system with both instant and sustainable anti-bacterial ability. *Nano Energy* **2017**, *36*, 241-249.

[59]   Lin, L.; Wang, S. H.; Niu, S. M.; Liu, C.; Xie, Y. N.; Wang, Z. L. Noncontact free-rotating disk triboelectric nanogenerator as a sustainable energy harvester and self-powered mechanical sensor. *ACS Appl. Mater. Interfaces* **2014**, *6*, 3031-3038.

[60]   Han, C. B.; Zhang, C.; Tang, W.; Li, X. H.; Wang, Z. L. High power triboelectric nanogenerator based on printed circuit board (PCB) technology. *Nano Res.* **2014**, *8*, 722-730.

[61]   Bi, M. Z.; Wang, S. W.; Wang, X. F.; Ye, X. Y. Freestanding-electret rotary generator at an average conversion efficiency of 56%: Theoretical and experimental studies. *Nano Energy* **2017**, *41*, 434-442.

[62]   Wu, C. S.; Tetik, H.; Cheng, J.; Ding, W. B.; Guo, H. Y.; Tao, X. T.; Zhou, N. J.; Zi, Y. L.; Wu, Z. Y.; Wu, H. X.; Lin, D.; Wang, Z. L. Electrohydrodynamic Jet Printing Driven by a Triboelectric Nanogenerator. *Adv. Funct. Mater.* **2019**, *29*, 1901102.

[63]   Wu, Z. B.; Bi, M. Z.; Cao, Z. Y.; Wang, S. W.; Ye, X. Y. Largely enhanced electrostatic generator based on a bipolar electret charged by patterned contact micro-discharge and optimized substrates. *Nano Energy* **2020**, *71*, 104602.

[64]   Jin, X.; Yuan, Z. H.; Shi, Y. P.; Sun, Y. G.; Li, R. N.; Chen, J. H.; Wang, L. F.; Wu, Z. Y.; Wang, Z. L. Triboelectric Nanogenerator Based on a Rotational Magnetic Ball for Harvesting Transmission Line Magnetic Energy. *Adv. Funct. Mater.* **2021**, *32*, 2108827.

[65]   Han, K.; Luo, J.; Chen, J.; Chen, B.; Xu, L.; Feng, Y.; Tang, W.; Wang, Z. L. Self-powered ammonia synthesis under ambient conditions via N2 discharge driven by Tesla turbine triboelectric nanogenerators. *Microsyst Nanoeng* **2021**, *7*, 7.

[66]   Wang, Y. Q.; Liu, X. Z.; Zheng, Z. H.; Yin, Y. J.; Wang, X. F.; You, Z. Numerical analysis and structural optimization of cylindrical grating-structured triboelectric nanogenerator. *Nano Energy* **2021**, *90*, 106570.

[67]   Kim, J.; Cho, H.; Han, M.; Jung, Y.; Kwak, S. S.; Yoon, H. J.; Park, B.; Kim, H.; Kim, H.; Park, J.; Kim, S. W. Ultrahigh Power Output from Triboelectric Nanogenerator Based on Serrated Electrode via Spark Discharge. *Adv. Energy Mater.* **2020**, *10*, 2002312.

Xuhua Guo is currently a M.S. student at Ocean University of China, His research mainly focuses on high-voltage applications of triboelectric nanogenerators and self-powered system.

Jianwei He is currently a M.S. student at Ocean University of China, His research mainly focuses on high-voltage applications of triboelectric nanogenerators and self-powered systems.

Prof. Caofeng Pan received his B.S. degree (2005) and PhD degree (2010) in Materials Science and Engineering from the Tsinghua University, China. He then joined the group of Prof. Zhong Lin Wang at the Georgia Institute of Technology as a postdoctoral fellow from 2010 to 2013. He is currently a professor and a group leader at the Beijing Institute of Nanoenergy and Nanosystems, CAS. His research interests mainly focus on piezotronics/piezophototronics for new electronic and optoelectronics, nanopower sources, hybrid nanogenerators, and self-powered nanosystems.

Prof. Yunlong Zi is an Assistant Professor in the Department of Mechanical and Automation Engineering at the Chinese University of Hong Kong. Dr. Zi received his Ph.D. in Physics from Purdue University in 2014; his Bachelor of Engineering in Materials Science and Engineering from Tsinghua University in 2009. Before joining CUHK, he worked as a Postdoctoral Fellow at the Georgia Institute of Technology during 2014–2017. His current research interests focus on high-efficiency mechanical energy harvesting through triboelectric nanogenerators), TENG triggered high-voltage applications and self-powered systems.

Prof. Hongzhi Cui received her B.S. degree from Shandong University in 1986. She received her M.S. degree from Shandong University in 1989. She received her Ph.D. degree from China University of Petroleum (East China) in 2009. She was a senior research scholar at Northwestern University, USA, during 2013–2014. She is currently a professor in the School of Materials Science and Engineering at the Ocean University of China. Her main research interests include the design of corrosion and wear-resistant materials for extreme environments, porous materials, seawater desalination, mechanical energy harvesting, high-voltage applications of triboelectric nanogenerators, and self-powered system.

Prof. Xiaoyi Li received his B. Eng. Degree from Southeast University in 2012. He received his Ph.D. degree in Materials Science and Engineering from Tsinghua University in 2017. He is also an exchange Ph.D. student at the Beijing Institute of Nanoenergy and Nanosystems (China Academy of Sciences) during 2013–2018. After his graduate study, Dr. Li joined the Chinese University of Hong Kong as a postdoctoral fellow of the Nano Energy and Smart System laboratory from 2018 to 2019. He is currently a professor in the School of Materials Science and Engineering at the Ocean University of China. His current research interests include mechanical energy harvesting, high-voltage applications of triboelectric nanogenerators, and self-powered systems.